Cross-scale interaction of host tree size and climate governs bark beetle-induced tree mortality

Keywords: Dendroctonus brevicomis, disturbance, drones, *Pinus ponderosa*, Sierra Nevada, structure from motion, forest structure, climate change-type drought, macroecology

Abstract word count: 310

Overall .docx word count: 11499

Main text word count: 4034 (Intro: 1264 Results: 368 (41+110+217); Discussion: 2402)

Methods word count: 3093 (661+642+1463+327)

Text boxes word count: 0

Date report generated: January 06, 2020

Abstract

The Californian hot drought of 2012 to 2015 created favorable conditions for unprecedented ponderosa pine (*Pinus ponderosa*) mortality in the Sierra Nevada mountain range, largely attributable to the western pine beetle (*Dendroctonus brevicomis*; WPB). Climate conditions and forest density may interact to affect tree mortality, but density is a coarse gauge of forest structure that can affect WPB behavior in a number of ways. Measuring broad-scale climate conditions simultaneously with local forest composition and structure– the spatial distribution and size of trees– will refine our understanding of how these variables interact, but is generally expensive and/or labor-intensive. We use drone surveys over a network of 160 field plots along a 350-km latitudinal and 1000-m elevational gradient in western slope Sierra Nevada ponderosa pine/mixed-conifer forests and structure from motion (SfM) processing to segment and classify more than 450,000 trees over 9 km^2 of forest with WPB-induced tree mortality. We modeled the probability of ponderosa pine mortality as a function of forest structure and composition and their interaction with site-level climatic water deficit (CWD), accounting for spatial covariance using exact Gaussian processes. A greater local proportion of host trees strongly increased the probability of host mortality, with greater host density amplifying this effect. Further, we found a strong interaction between host size and CWD such that larger trees increased the probability of host mortality at hot/dry sites, but smaller trees tended to drive mortality in cool/wet sites.

Our results demonstrate a variable response of WPB to local forest structure and composition across an environmental gradient, which may help reconcile differences between observed ecosystem-wide tree mortality patterns and predictions from models based on coarser-scale forest structure. Climate change adaptation strategies should consider that future disturbance outcomes may depend on interactions between local forest

structure and broad-scale environmental gradients, with the potential for cross-scale interactions that challenge our current understanding of forest insect dynamics.

Introduction

Bark beetles dealt the final blow to many of the nearly 150 million trees killed in the California hot drought of 2012 to 2015 and its aftermath (USDAFS 2019). A harbinger of climate change effects to come, record high temperatures exacerbated the drought (Griffin and Anchukaitis 2014), which increased water stress in trees (Asner et al. 2016), making them more susceptible to colonization by bark beetles (Fettig 2012, Kolb et al. 2016). Further, a century of fire suppression policy has enabled forests to grow into dense stands, which can also makes them more vulnerable to bark beetles (Fettig 2012). This combination of environmental conditions and forest structural characteristics led to tree mortality events of unprecedented size in the driest, densest forests across the state (Young et al. 2017). The mechanisms underlying the link between tree susceptibility to colonization by insects and hot, dry conditions are often directly attributed to tree physiology (Bentz et al. 2010, Kolb et al. 2016), while the link to forest density is multifaceted (Fettig 2012). Because forest density is a coarse metric of the forest features to which bark beetles respond (Raffa et al. 2008), our understanding of the connection between forest density and insect disturbance severity could be enhanced with more finely-resolved measures of forest structure as well as explicit consideration of tree species composition (Stephenson et al. 2019, Fettig et al. 2019). Finally, the challenge of simultaneously measuring the effects of both local-scale forest features (such as structure and composition) and broad-scale environmental conditions (such as climatic water deicit; CWD) on forest insect disturbance leaves their interaction effect relatively underexplored (Seidl et al. 2016, Stephenson et al. 2019, Fettig et al. 2019).

The ponderosa pine/mixed-conifer forests in California's Sierra Nevada region are characterized by regular bark beetle disturbances, primarily by the influence of western pine beetle (*Dendroctonus brevicomis*; WPB) on its host ponderosa pine (*Pinus ponderosa*) (Fettig 2016). WPB is a "primary" bark beetle– its reproductive success is contingent upon host tree mortality, which itself requires enough beetles to "mass attack" the host tree and overwhelm its defenses (Raffa and Berryman 1983). This Allee effect creates a strong coupling between beetle selection behavior of host trees and host tree susceptibility to colonization (Raffa and Berryman 1983, Logan et al. 1998). A key defense mechanism of conifers to bark beetle attack is to flood beetle bore holes with resin, which physically expels beetles and may interrupt beetle communication (Franceschi et al. 2005, Raffa et al. 2015). Under normal conditions, weakened trees with compromised defenses are the most susceptible to colonization and will be the main targets of primary bark beetles like WPB (Bentz et al. 2010, Raffa et al. 2015). Under severe water stress, many trees no longer have the resources available to mount

a defense (Kolb et al. 2016) and thus prolonged drought can often trigger increased bark beetle-induced tree mortality as average tree vigor declines (Bentz et al. 2010). As the local population density of beetles increases due to successful reproduction within spatially-aggregated weakened trees, as might occur during drought, mass attacks grow in size and become capable of overwhelming formidable tree defenses such that even healthy trees may be susceptible to colonization and mortality (Bentz et al. 2010, Raffa et al. 2015). Thus, water stress can be a key determinant of whether individual trees are susceptible to bark beetles under many conditions, and this environmental condition may interact with beetle population dynamics to drive tree susceptibility under extreme conditions (Bentz et al. 2010, Stephenson et al. 2019).

WPB activity is strongly influenced by forest structure– the spatial distribution and size of trees– and tree species composition. Taking forest structure alone, high-density forests are more prone to bark beetle-induced tree mortality (Fettig 2012) which may arise as greater competition for water resources amongst crowded trees and thus average tree resistance is lower (Hayes et al. 2009), or because smaller gaps between trees protect pheromone plumes from dissipation by the wind and thus enhance intraspecific beetle communication (Thistle et al. 2004). Tree size is another aspect of forest structure that affects bark beetle host selection behavior with smaller trees tending to have lower capacity for resisting attack, and larger trees being more desirable targets on account of their thicker phloem providing greater nutritional content (Chubaty et al. 2009, Graf et al. 2012). Taking forest composition alone, WPB activity in the Sierra Nevada mountain range of California is necessarily tied to the regional distribution of its exclusive host, ponderosa pine (Fettig 2016). Colonization by primary bark beetles can also depend on the relative frequencies of tree species in a more local area, akin to reduced oligophagous insect herbivory in forests comprising taxonomically-distinct tree species compared to monocultures (Jactel and Brockerhoff 2007). The interaction between forest structure and composition also drives WPB activity. For instance, high-density forests with high host availability may experience greater beetle-induced tree mortality because dispersal distances between potential host trees are shorter reducing predation of adults searcing for hosts and facilitating higher rates of colonization (Miller and Keen 1960, Berryman 1982, Fettig et al. 2007) or because high host availability reduces the chance of individual beetles wasting their limited resources flying to and landing on a non-host tree (Moeck et al. 1981, Evenden et al. 2014). Stand-scale measures of forest structure and composition thus paint a fundamentally limited picture of the mechanisms by which these forest characteristics affect bark beetle disturbance, but finer-grain information explicitly recognizing tree size, tree species, and local tree density should more appropriately capture the ecological processes underlying insect-induced tree mortality. Additionally, considering the effects of local forest structure and composition with the effects of environmental conditions may help refine our understanding of tree mortality patterns in widespread events such as during the recent California hot

drought.

The vast spatial extent of tree mortality in the 2012 to 2015 California hot drought challenges our ability to simultaneously consider how broad-scale environmental conditions may interact with local forest structure and composition to affect the dynamic between bark beetle selection and colonization of host trees, and host tree susceptibility to attack (Anderegg et al. 2015, Stephenson et al. 2019). Measuring local forest structure generally requires expensive instrumentation (Kane et al. 2014, Asner et al. 2016) or labor-intensive field surveys (Larson and Churchill 2012, Stephenson et al. 2019, Fettig et al. 2019), which constrains survey extent and frequency. Small, unhumanned aerial systems (sUAS) enable relatively fast and cheap remote imaging over dozens of hectares of forest, which can be used to measure complex forest structure at the individual tree scale (Morris et al. 2017, Shiklomanov et al. 2019). Distributing such surveys across an environmental gradient can overcome the data acquisition challenge inherent in investigating phenomena with both a strong local- and a strong broad-scale component.

We used ultra-high resolution, sUAS-derived remote sensing data over a network of 32 sites in Sierra Nevada ponderosa pine/mixed-conifer forests spanning 1000 m of elevation and 350 km of latitude (see Fettig et al. 2019) and covering a total of 9 km^2 to ask how broad-scale environmental conditions interacted with local forest structure and composition to affect the probability of tree mortality during the cumulative tree mortality event of 2012 to 2018. We asked:

1. How does the proportion of host trees in a local area and average host tree size affect WPB-induced tree mortality?
2. How does the density of all tree species (hereafter "overall density") affect WPB-induced tree mortality?
3. How does environmentally-driven tree moisture stress affect WPB-induced tree mortality?
4. Do the effects of forest structure, forest composition, and environmental condition interact to influence WPB-induced tree mortality?

Methods

Study system

We built our study coincident with 160 vegetation/forest insect monitoring plots at 32 sites established between 2016 and 2017 by Fettig et al. (2019) (Figure 1). The study sites were chosen to reflect typical west-side Sierra Nevada yellow pine/mixed-conifer forests and were dominated by ponderosa pine (Fettig et al. 2019). Plots were located in WPB-attacked, yellow pine/mixed-conifer forests across the Eldorado,

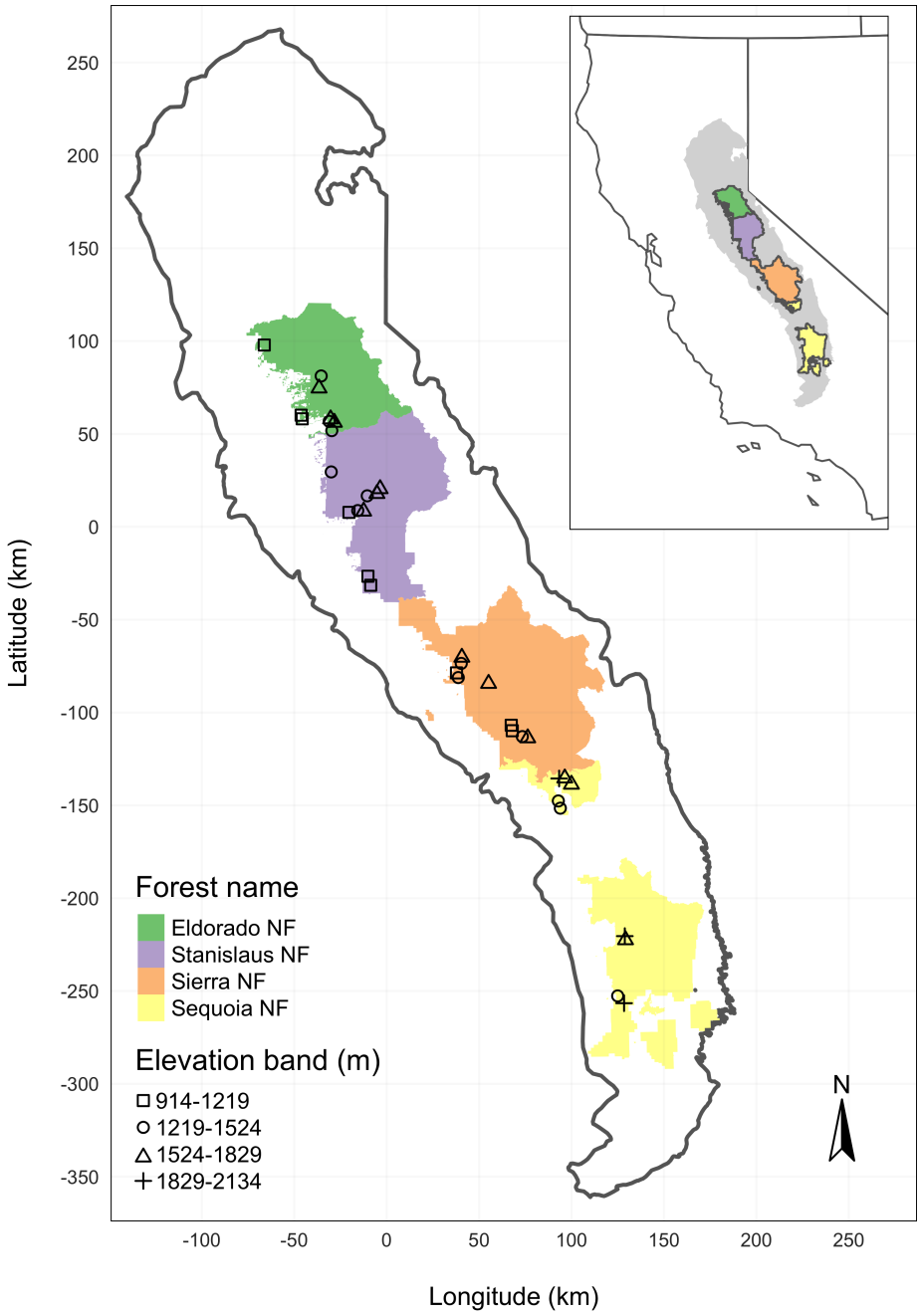

Figure 1: The network of field plots spanned a 350-km latitudinal gradient from the Eldorado National Forest in the north to the Sequoia National Forest in the south. Plots were stratified by three elevation bands in each forest, with the plots in the Sequoia National Forest (the southern-most National Forest) occupying elevation bands 305 m above the three bands in the other National Forests in order to capture a similar community composition.

Stanislaus, Sierra and Sequoia National Forests and were stratified by elevation (914-1219 m, 1219-1524 m, 1524-1829 m above sea level). In the Sequoia National Forest, the southernmost National Forest in our study, plots were stratified with the lowest elevation band of 1219-1524 m and extended to an upper elevation band of 1829-2134 m to capture a more similar forest community composition as at the more northern National Forests. The sites have variable forest structure and plot locations were selected in areas with >35% ponderosa pine basal area and >10% ponderosa pine mortality. At each site, five 0.041 ha circular plots were installed along transects with 80 to 200m between plots. In the field, Fettig et al. (2019) mapped all stem locations relative to the center of each plot using azimuth/distance measurements. Tree identity to species, tree height, and diameter at breast height (DBH) were recorded if DBH was greater than 6.35cm. Year of mortality was estimated based on needle color and retention if it occurred prior to plot establishment, and was directly observed thereafter during annual site visits. A small section of bark (approximately 625 cm^2) on both north and south aspects was removed from dead trees to determine if bark beetle galleries were present. The shape, distribution, and orientation of galleries are commonly used to distinguish among bark beetle species (Fettig 2016). In some cases, deceased bark beetles were present beneath the bark to supplement identifications based on gallery formation. During the spring and early summer of 2018, all field plots were revisited to assess whether dead trees had fallen (Fettig et al. 2019).

In the typical life cycle of WPBs, females initiate host colonization by tunneling through the outer bark and into the phloem and outer xylem where they rupture resin canals.

As a result, oleoresin exudes and collects on the bark surface, as is commonly observed with other bark beetle species. During the early stages of attack, females release an aggregation pheromone component which, in combination with host monoterpenes released from pitch tubes, is attractive to conspecifics (Bedard et al. 1969). An antiaggregation pheromone component is produced during latter stages of host colonization by several pathways, and is thought to reduce intraspecific competition by altering adult behavior to minimize overcrowding of developing brood within the host (Byers and Wood 1980). Volatiles from several nonhosts sympatric with ponderosa pine have been demonstrated to inhibit attraction of WPB (Shepherd et al. 2007, Fettig and Hilszczański 2015). In California, WPB generally has 2-3 generations in a single year and can often out-compete its congener, the mountain pine beetle, *Dendroctonus ponderosae*, in ponderosa pines, especially in larger trees (Miller and Keen 1960).

Aerial data collection and processing

Nadir-facing imagery was captured using a gimbal-stabilized DJI Zenmuse X3 broad-band red/green/blue (RGB) camera (DJI 2015a) and a fixed-mounted Micasense Rededge3 multispectral camera with five narrow

bands (Micasense 2015) on a DJI Matrice 100 aircraft (DJI 2015b). Imagery was captured from both cameras along preprogrammed aerial transects over ~40 hectares surrounding each of the 32 sites (each of these containing five field plots) and was processed in a series of steps to yield local forest structure and composition data suitable for our statistical analyses. Following the call by Wyngaard et al. (2019), we establish "data product levels" to reflect the image processing pipeline from raw imagery (Level 0) to calibrated, fine-scale forest structure and composition information on regular grids (Level 4), with each new data level derived from levels below it. Here, we outline the steps in the processing and calibration pipeline visualized in Figure 2, and include additional details in the Supplemental Information.

Level 0: raw data from sensors

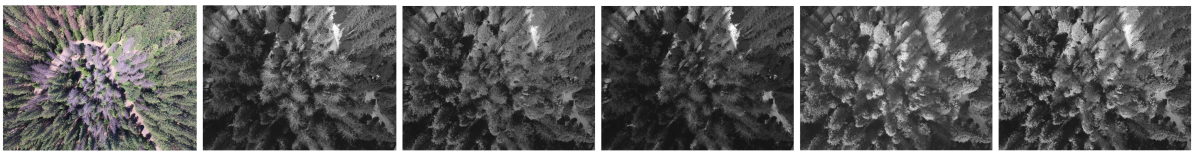

Level 1: basic outputs from photogrammetric processing

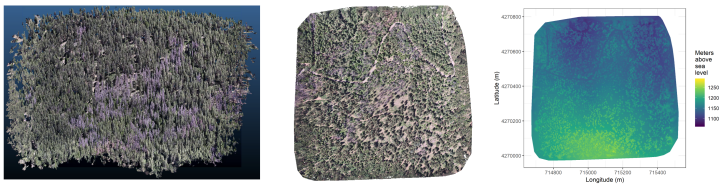

Level 2: corrected outputs from photogrammetric processing

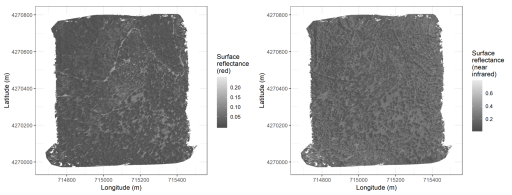

radiometric (e.g., normalize for atmosphere)

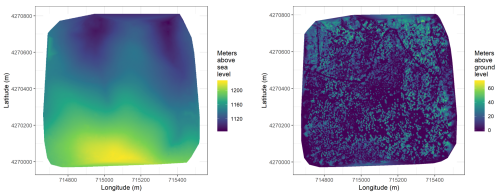

geometric (e.g., normalize for terrain)

Level 3: domain-specific information extraction

L3a
spectral
OR
geometric

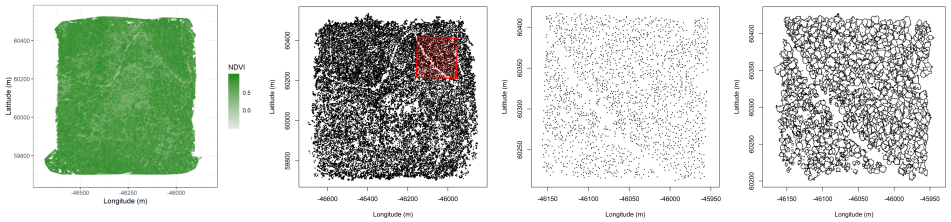

L3b
spectral
AND
geometric

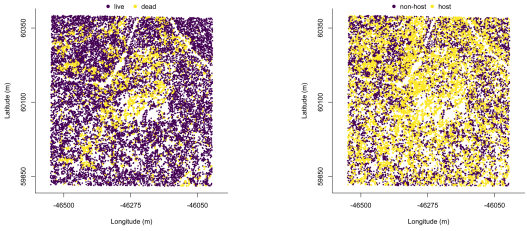

Level 4: aggregations to regular grids

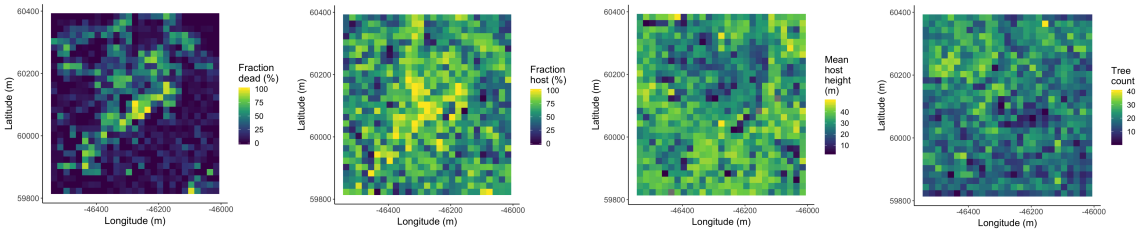

Figure 2. Schematic of the data processing workflow for a single site with each new data product level derived from data at lower levels.

Level 0 represents raw data from the sensors. From left to right: example broad-band RGB photo from DJI Zenmuse X3 camera, example blue photo from Rededge3 (centered on 475nm), example green photo from Rededge3 (centered on 560nm), example red photo from Rededge3 (centered on 668nm), example near infrared photo from Rededge3 (centered on 840nm), and example red edge photo from Rededge3 (centered on 717nm).

Level 1 represents basic outputs from the photogrammetric workflow, in this case implemented with Pix4Dmapper. From left to right: a dense point cloud visualized in CloudCompare (https://www.danielgm.net/cc/), an orthophoto generated from the RGB camera, and a digital surface model representing the altitude above sea level (ground height + vegetation height) for every cell.

Level 2 represents outputs from photogrammetric processing that have been corrected radiometrically or geometrically. From left to right: a radiometrically-corrected surface reflectance map of the red narrow band from the Rededge3 camera, a radiometrically-corrected surface reflectance map of the near infrared narrow band from the Rededge3 camera, a rasterized version of the digital terrain model derived by a geometric correction of the dense point cloud, and a canopy height model derived by subtracting the terrain height from the digital surface model.

Level 3 represents domain-specific information extraction from Level 2 products and is divided into two sub-levels. Level 3a products are derived using only spectral or only geometric data. From left to right: a reflectance map of Normalized Difference Vegetation Index (NDVI; Rouse et al. (1973)) derived using the red and near infrared Level 2 reflectance products, a map of points representing detected trees from the canopy height model with a red polygon highlighting the area presented in more detail for the next two images, a close-up of points representing detected trees, and a close-up of polygons representing segmented tree crowns. Level 3b products are derived using both spectral and geometric data. From left to right: a map of the point locations of detected trees that have been classified as alive or dead based on the pixel values within each segmented tree crown and a map of the point locations of detected trees classified to WPB host/non-host using the same spectral information. Note that our study relies on the generation of Level 3a products in order to combine them and create Level 3b products, but this need not be the case. For instance, deep learning/neural net methods may be able to use both the spectral and geometric information from Level 2 simultaneously to locate and classify trees in a scene and directly generate Level 3b products without a need to first generate the Level 3a products shown in this schematic (Weinstein et al. 2019, dos Santos et al. 2019).

Level 4 represents aggregations of Level 3 products to regular grids which might better reflect the grain size of the data for which we have the best calibration and thus the most confidence or which might provide new information not possible at an individual-tree level (e.g., average distance between trees in a small neighborhood). From left to right: aggregation of live/dead classified trees as fraction of dead trees in a 20 x 20-m cell, aggregation of host/non-host classified trees as fraction of hosts in a 20 x 20-m cell, aggregation of mean host height in a 20 x 20-m cell, and aggregation of tree count (including all species), in a 20 x 20-m cell. In our case, the 20 x 20-m aggregation produces a grid cell with an area of 400 m^2, which most closely matches the 404-m^2 area of the ground-based vegetation plots whose data we used in an aggregated form to calibrate our derivation of Level 3 products.

Level 0: Raw data from sensors

Raw data comprised approximately 1900 images per camera lens (one broad-band RGB lens and five narrow-band multispectral lenses) for each of the 32 sites (Figure 2; Level 0). Prior to the aerial survey, two strips of bright orange drop cloth (~100 x 15 cm) were positioned as an "X" over the permanent monuments marking the center of the 5 field plots from Fettig et al. (2019) (see Supplemental Information).

We preprogrammed north-south aerial transects using Map Pilot for DJI on iOS flight software (DronesMadeEasy 2018) at an altitude of 120 m above ground level (with "ground" defined using a 1-arc-second digital elevation model (Farr et al. 2007)). The resulting ground sampling distance was approximately 5 cm/px for the Zenmuse X3 RGB camera and approximately 8 cm/px for the Rededge3 multispectral camera. We used 91.6% image overlap (both forward and side) at the ground for the Zenmuse X3 RGB camera and 83.9% overlap (forward and side) for the Rededge3 multispectral camera.

Level 1: Basic outputs from photogrammetric processing

We used SfM photogrammetry implemented in Pix4Dmapper Cloud (www.pix4d.com) to generate dense point clouds (Figure 2; Level 1, left), orthophotos (Figure 2; Level 1, center), and digital surface models (Figure 2; Level 1, right) for each field site (Frey et al. 2018). For 29 sites, we processed the Rededge3 multispectral imagery alone to generate these products. For three sites, we processed the RGB and the multispectral imagery together to enhance the point density of the dense point cloud. All SfM projects resulted in a single processing "block," indicating that all images in the project were optimized and processed together. The dense point cloud represents x, y, and z coordinates as well as the color of millions of points per site. The orthophoto represents a radiometrically uncalibrated, top-down view of the survey site that preserves the relative x-y positions of objects in the scene. The digital surface model is a rasterized version of the dense

point cloud that shows the altitude above sea level for each pixel in the scene at the ground sampling distance of the camera that generated the Level 0 data.

Level 2: Corrected outputs from photogrammetric processing

Radiometric corrections

A radiometrically-corrected reflectance map (Figure 2; Level 2, left two figures; i.e., a corrected version of the Level 1 orthophoto) was generated using the Pix4D software by incorporating incoming light conditions for each narrow band of the Rededge3 camera (captured simultaneously with the Rededge3 camera using an integrated downwelling light sensor) as well as a pre-flight image of a calibration panel of known reflectance (see Supplemental Information for camera and calibration panel details).

Geometric corrections

We implemented a geometric correction to the Level 1 dense point cloud and digital surface model by normalizing these data for the terrain underneath the vegetation. We generated the digital terrain model representing the ground underneath the vegetation at 1-m resolution (Figure 2; Level 2, third image) by classifying each survey area's dense point cloud into "ground" and "non-ground" points using a cloth simulation filter algorithm (Zhang et al. 2016) implemented in the `lidR` (Roussel et al. 2019) package and rasterizing the ground points using the `raster` package (Hijmans et al. 2019). We generated a canopy height model (Figure 2; Level 2, fourth image) by subtracting the digital terrain model from the digital surface model.

Level 3: Domain-specific information extraction

Level 3a: Data derived from spectral OR geometric Level 2 product

Using just the spectral information from the radiometrically-corrected reflectance maps, we calculated several vegetation indices including the normalized difference vegetation index (NDVI; Rouse et al. (1973); Figure 2; Level 3a, first image), the normalized difference red edge (NDRE; Gitelson and Merzlyak (1994)), the red-green index (RGI; Coops et al. (2006)), the red edge chlorophyll index ($CI_{\text{red edge}}$; Clevers and Gitelson (2013)), and the green chlorophyll index (CI_{green}; Clevers and Gitelson (2013)).

Table 1: Algorithm name, number of parameter sets tested for each algorithm, and references.

Algorithm	Parameter sets tested	Reference(s)
li2012	131	Li et al. (2012); Jakubowski et al. (2013); Shin et al. (2018)

Algorithm	Parameter sets tested	Reference(s)
lmfx	30	Roussel (2019)
localMaxima	6	Roussel et al. (2019)
multichm	1	Eysn et al. (2015)
ptrees	3	Vega et al. (2014)
vwf	3	Plowright (2018)
watershed	3	Pau et al. (2010)

Using just the geometric information from the canopy height model or terrain-normalized dense point cloud, we generated maps of detected trees (Figure 2; Level 3a, second and third images) by testing a total of 7 automatic tree detection algorithms and a total of 177 parameter sets (Table 1). We used the field plot data to assess each tree detection algorithm/parameter set by converting the distance-from-center and azimuth measurements of the trees in the field plots to x-y positions relative to the field plot centers distinguishable in the Level 2 reflectance maps as the orange fabric X's that we laid out prior to each flight. In the reflectance maps, we located 110 out of 160 field plot centers while some plot centers were obscured due to dense interlocking tree crowns or because a plot center was located directly under a single tree crown. For each of the 110 field plots with identifiable plot centers– the "validation field plots", we calculated 7 forest structure metrics using the ground data collected by Fettig et al. (2019): total number of trees, number of trees greater than 15 m in height, mean height of trees, 25^{th} percentile tree height, 75^{th} percentile tree height, mean distance to nearest tree neighbor, and mean distance to second nearest neighbor. For each tree detection algorithm and parameter set described above, we calculated the same set of 7 structure metrics within the footprint of the validation field plots. We calculated the Pearson's correlation and root mean square error (RMSE) between the ground data and the aerial data for each of the 7 structure metrics for each of the 177 automatic tree detection algorithms/parameter sets. For each algorithm and parameter set, we calculated its performance relative to other algorithms as whether its Pearson's correlation was within 5% of the highest Pearson's correlation as well as whether its RMSE was within 5% of the lowest RMSE. We summed the number of forest structure metrics for which it reached these 5% thresholds for each algorithm/parameter set. For automatically detecting trees across the whole study, we selected the algorithm/parameter set that performed well across the most number of forest metrics (see Results).

We delineated individual tree crowns (Figure 2; Level 3a, fourth image) with a marker controlled watershed segmentation algorithm (Meyer and Beucher 1990) implemented in the `ForestTools` package (Plowright

2018) using the detected treetops as markers. If the automatic segmentation algorithm failed to generate a crown segment for a detected tree (e.g., often snags with a very small crown footprint), a circular crown was generated with a radius of 0.5 m. If the segmentation generated multiple polygons for a single detected tree, only the polygon containing the detected tree was retained. Because image overlap decreases near the edges of the overall flight path and reduces the quality of the SfM processing in those areas, we excluded segmented crowns within 35 m of the edge of the survey area. Given the narrower field of view of the Rededge3 multispectral camera versus the X3 RGB camera whose optical parameters were used to define the ~40 hectare survey area around each site, as well as the 35 m additional buffering, the survey area at each site was ~30 ha (see Supplemental Information).

Level 3b: Data derived from spectral AND geometric information

We overlaid the segmented crowns on the reflectance maps from 20 sites spanning the latitudinal and elevation gradient in the study. Using QGIS (https://qgis.org/en/site/), we hand classified 564 trees as live/dead (Figure 3) and as one of 5 dominant species in the study area (ponderosa pine, *Pinus lambertiana*, *Abies concolor*, *Calocedrus decurrens*, or *Quercus kelloggi*) using the mapped ground data as a guide. Each tree was further classified as "host" for ponderosa pine or "non-host" for all other species (Fettig 2016). We extracted all the pixel values within each segmented crown polygon from the five, Level 2 orthorectified reflectance maps (one per narrow band on the Rededge3 camera) as well as from the five, Level 3a vegetation index maps using the `velox` package (Hunziker 2017). For each crown polygon, we calculated the mean value of the extracted Level 2 and Level 3a pixels and used them as ten independent variables in a five-fold cross validated boosted logistic regression model to predict whether the hand classified trees were alive or dead. For just the living trees, we similarly used all 10 mean reflectance values per crown polygon to predict tree species using a five-fold cross validated regularized discriminant analysis. The boosted logistic regression and regularized discriminant analysis were implemented using the `caret` package in R (Kuhn 2008). Finally, we used these models to classify all tree crowns in the data set as alive or dead (Figure 2; Level 3b, first image) as well as the species of living trees (Figure 2; Level 3b, second image).

Level 4: Aggregations to regular grids

We rasterized the forest structure and composition data at a spatial resolution similar to that of the field plots to better match the grain size at which we validated the automatic tree detection algorithms. In each raster cell, we calculated: number of dead trees, number of ponderosa pine trees, total number of trees, and mean height of ponderosa pine trees. The values of these variables in each grid cell and derivatives from them were used for visualization and modeling. Here, we show the fraction of dead trees per cell (Figure 2;

Level 4, first image), the fraction of host trees per cell (Figure 2; Level 4, second image), the mean height of ponderosa pine trees in each cell (Figure 2; Level 4, third image), and the total count of trees per cell (Figure 2; Level 4, fourth image).

Note on assumptions about dead trees

For the purposes of this study, we assumed that all dead trees were ponderosa pine and thus hosts colonized by WPB. This is a reasonably good assumption for our study area; for example, Fettig et al. (2019) found that 73.4% of dead trees in their coincident field plots were ponderosa pine. Mortality was concentrated in the larger-diameter classes and attributed primarily to WPB (see Figure 5 of Fettig et al. 2019). The species contributing to the next highest proportion of dead trees was incense cedar which represented 18.72% of the dead trees in the field plots. While the detected mortality is most likely to be ponderosa pine killed by WPB, it is critical to interpret our results with these limitations in mind.

Environmental data

We used CWD (Stephenson 1998) from the 1981-2010 mean value of the basin characterization model (Flint et al. 2013) as an integrated measure of temperature and moisture conditions for each of the 32 sites. Higher values of CWD correspond to hotter, drier conditions and lower values correspond to cooler, wetter conditions. CWD has been shown to correlate well with broad patterns of tree mortality in the Sierra Nevada (Young et al. 2017) as well as bark beetle-induced tree mortality (Millar et al. 2012). We converted the CWD value for each site into a z-score representing that site's deviation from the mean CWD across the climatic range of Sierra Nevada ponderosa pine as determined from 179 herbarium records described in Baldwin et al. (2017). Thus, a CWD z-score of 1 would indicate that the CWD at that site is one standard deviation hotter/drier than the mean CWD across all geolocated herbarium records for ponderosa pine in the Sierra Nevada.

Statistical model

We used a generalized linear model with a zero-inflated binomial response and a logit link to predict the probability of ponderosa pine mortality within each 20 x 20-m cell using the total number of ponderosa pine trees in each cell as the number of trials, and the number of dead trees in each cell as the number of "successes". As covariates, we used the proportion of trees that are WPB hosts (i.e., ponderosa pine) in each cell, the mean height of ponderosa pine trees in each cell, the count of trees of all species (overall density) in each cell, and the site-level CWD using Eq. 1. Note that the two-way interaction between the overall density and the proportion of trees that are hosts is equivalent to the number of ponderosa pine trees in the cell. To measure and account for spatial autocorrelation underlying ponderosa pine mortality, we subsampled

the data at each site to a random selection of 200, 20 x 20-m cells representing approximately 27.5% of the surveyed area. Additionally with these subsampled data, we included a separate exact Gaussian process term per site of the interaction between the x- and y-position of each cell using the `gp()` function in the `brms` package (Bürkner 2017). The Gaussian process estimates the spatial covariance in the response variable (log-odds of ponderosa pine mortality) jointly with the effects of the other covariates.

$$y_{i,j} \sim \begin{cases} 0, & p \\ Binom(n_i, \pi_i), & 1-p \end{cases}$$

$$\begin{aligned} logit(\pi_i) = \beta_0 + & \\ & \beta_1 X_{cwd,j} \ + \beta_2 X_{propHost,i} + \beta_3 X_{PIPOheight,i} + \beta_4 X_{overallDensity,i} + \\ & \beta_5 X_{cwd,j} X_{PIPOheight,i} + \beta_6 X_{cwd,j} X_{propHost,i} + \beta_7 X_{cwd,j} X_{overallDensity,i} + \\ & \beta_8 X_{propHost,i} X_{PIPOheight,i} + \beta_9 X_{propHost,i} X_{overallDensity,i} + \\ & \beta_{10} X_{cwd,j} X_{propHost,i} X_{PIPOheight,i} + \\ & \mathcal{GP}_j(x_i, y_i) \end{aligned}$$

Where y_i is the number of dead trees in cell i, n_i is the sum of the dead trees (assumed to be ponderosa pine) and live ponderosa pine trees in cell i, π_i is the probability of ponderosa pine tree mortality in cell i, p is the probability of there being zero dead trees in a cell arising as a result of an unmodeled process, $X_{cwd,j}$ is the z-score of CWD for site j, $X_{propHost,i}$ is the scaled proportion of trees that are ponderosa pine in cell i, $X_{PIPOheight,i}$ is the scaled mean height of ponderosa pine trees in cell i, $X_{overallDensity,i}$ is the scaled density of all trees in cell i, x_i and y_i are the x- and y- coordinates of the centroid of the cell in an EPSG3310 coordinate reference system, and $\mathcal{GP}_j$ represents the exact Gaussian process describing the spatial covariance between cells at site j.

We used 4 chains with 4000 iterations each (2000 warmup, 2000 samples), and confirmed chain convergence by ensuring all `Rhat` values were less than 1.1 (Brooks and Gelman 1998) and that the bulk and tail effective sample sizes (ESS) for each estimated parameter were greater than 100 times the number of chains (i.e., greater than 400 in our case). We used posterior predictive checks to visually confirm model performance by overlaying the density curves of the predicted number of dead trees per cell over the observed number (Gabry et al. 2019). For the posterior predictive checks, we used 50 random samples from the model fit to generate 50 density curves and ensured curves were centered on the observed distribution, paying special attention to model performance at capturing counts of zero.

Software and data availability

All data are available via the Open Science Framework. Statistical analyses were performed using the `brms` packages. With the exception of the SfM software (Pix4Dmapper Cloud) and the GIS software QGIS, all data carpentry and analyses were performed using `R` (R Core Team 2018).

Results

Tree detection algorithm performance

We found that the experimental `lmfx` algorithm with parameter values of `dist2d = 1` and `ws = 2.5` (Roussel et al. 2019) performed the best across 7 measures of forest structure as measured by Pearson's correlation with ground data (Table 2).

Table 2: Correlation and differences between the best performing tree detection algorithm (lmfx with dist2d = 1 and ws = 2.5) and the ground data. An asterisk next to the correlation or RMSE indicates that this value was within 5% of the value of the best-performing algorithm/parameter set. Ground mean represents the mean value of the forest metric across the 110 field plots that were visible from the sUAS-derived imagery. The median error is calculated as the median of the differences between the air and ground values for the 110 visible plots. Thus, a positive number indicates an overestimate by the sUAS workflow and a negative number indicates an underestimate.

Forest structure metric	Ground mean	Correlation with ground	RMSE	Median error
total tree count	19	0.67*	8.68*	2
count of trees > 15 m	9.9	0.43	7.38	0
distance to 1st neighbor (m)	2.8	0.55*	1.16*	0.26
distance to 2nd neighbor (m)	4.3	0.61*	1.70*	0.12
height (m); 25^{th} percentile	12	0.16	8.46	-1.2
height (m); mean	18	0.29	7.81*	-2.3
height (m); 75^{th} percentile	25	0.35	10.33*	-4

Classification accuracy for live/dead and host/non-host

The accuracy of live/dead classification on a withheld test dataset was 97.3%. The accuracy of species classification on a withheld testing dataset was 66.7%. The accuracy of WPB host/non-WPB-host (i.e., ponderosa pine versus other tree species) on a withheld testing dataset was 74.4%.

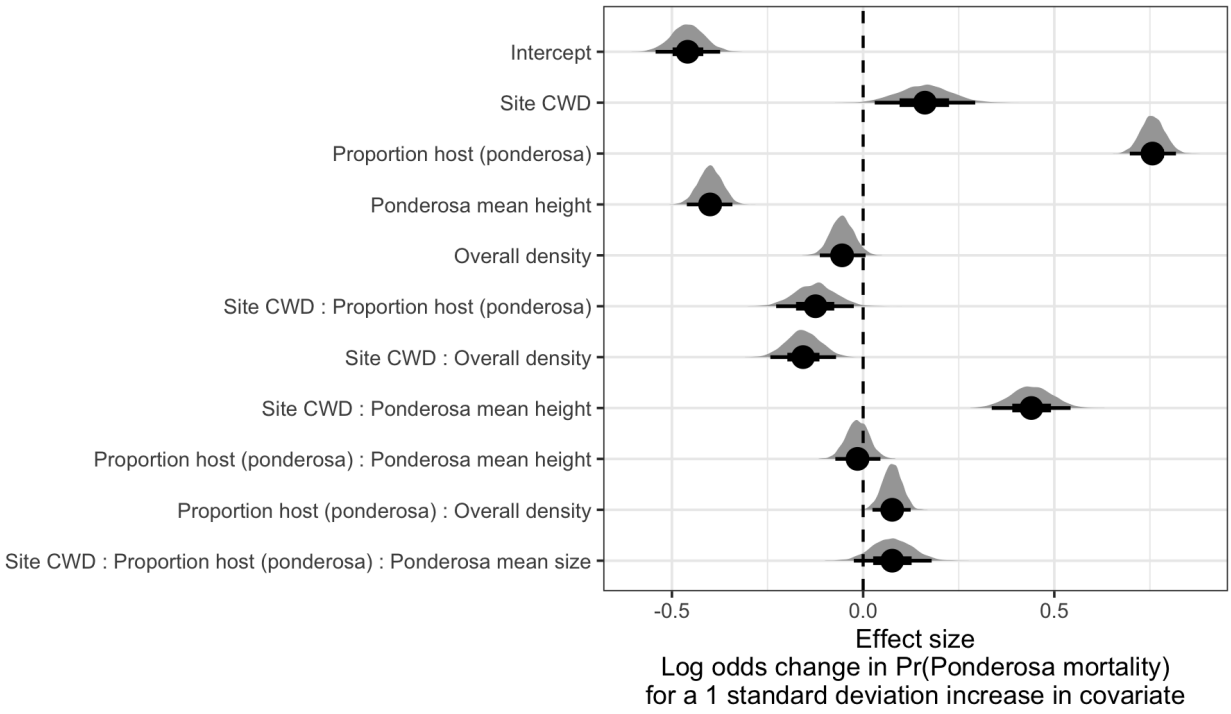

Figure 4: Posterior distributions of effect size from zero-inflated binomial model predicting the probability of ponderosa pine mortality in a 20 x 20-m cell given forest structure characteristics and site-level climatic water deficit (CWD). The gray density distribution for each model covariate represents the density of the posterior distribution, the point underneath each density curve represents the median of the estimate, the bold interval surrounding the point estimate represents the 66% credible interval, and the thin interval surrounding the point estimate represents the 95% credible interval.

Site summary based on best tree detection algorithm and classification

Across all study sites, we detected, segmented, and classified 452,413 trees (see Supplemental Information for site summaries). Of these trees, we classified 118,879 as dead (26.3% mortality). Estimated site-level tree mortality ranged from 6.8% to 53.6%.

Effect of local structure and regional climate on tree mortality attributed to western pine beetle

We detected a positive main effect of CWD on the probability of ponderosa pine mortality within each 20 x 20-m cell (Figure 4). We found a positive main effect of proportion of host trees per cell, with a greater proportion of host trees (i.e., ponderosa pine) in a cell increasing the probability of ponderosa pine mortality. Conversely, we found a negative effect of overall tree density (i.e., including both ponderosa pine and non-host species) such that greater tree density in a 20 x 20-m cell (for the same proportion of host trees) would decrease the probability of ponderosa pine mortality. We found a positive two-way interaction between the

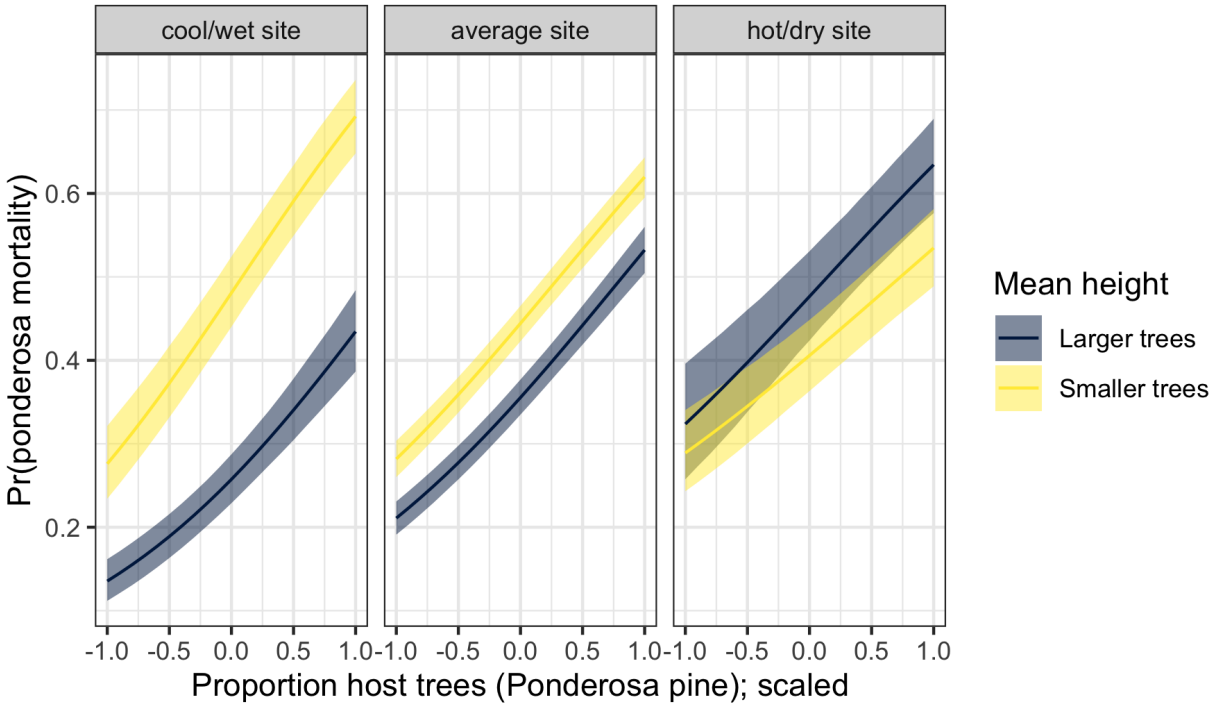

Figure 5: Line version of model results with 95% credible intervals showing primary influence of ponderosa pine structure on the probability of ponderosa pine mortality, and the interaction across climatic water deficit. The 'larger trees' line represents the mean height of ponderosa pine 0.7 standard deviations above the mean (approximately 24.1 m), and the 'smaller trees' line represents the mean height of ponderosa pine 0.7 standard deviations below the mean (approximately 12.1 m).

overall tree density per cell and the proportion of trees that were hosts, which is equivalent to a positive effect of the density of host trees (Figure 4).

We found a negative effect of mean height of ponderosa pine on the probability of ponderosa mortality, suggesting that WPB attacked smaller trees, on average. However, there was a positive interaction between CWD and ponderosa pine mean height, such that larger trees were more likely to increase the probability of ponderosa mortality in hotter, drier sites (Figure 5).

We found weakly negative effects of the site-level CWD interactions with both the proportion of host trees and overall tree density (Figure 4).

Discussion

This study represents a novel use of drones to further our understanding of the simultaneous effects of local forest structure and composition with broad-scale environmental gradients on tree mortality attributed to WPB. We found strong positive effects (effect sizes >0.4) of both the proportion of host trees and the interaction between site CWD and host tree mean size (height) on the probability of ponderosa pine mortality.

Conversely, we found a strong negative effect (effect size <-0.4) of mean height of ponderosa pine. Site-level CWD exerted a positive, but relatively weak, main effect on the probability of ponderosa mortality (effect size: 0.16; 95% CI: [0.03, 0.29]). To that end, we did not measure tree water stress at an individual tree level as in other recent work (Stephenson et al. 2019), and instead treated CWD as a general indicator of tree stress following results of coarser-scale studies (e.g., Asner et al. 2016, Young et al. 2017), which may have contributed to our failure to detect a stronger CWD effect. Also, our entire study area experienced the same extreme hot drought between 2012 and 2015 and the variation of mortality explained by a main effect of CWD may be dampened when most trees are experiencing a high degree of water stress (Floyd et al. 2009, Fettig et al. 2019).

Positive effect of host density and a negative effect of overall density

The strongest effect on the probability of ponderosa pine mortality was the positive effect of the proportion of trees in each 20 x 20-m cell that were ponderosa pine– the host of the WPB (effect size: 0.76; 95% CI: [0.70, 0.82]).

A number of mechanisms associated with the relative abundance of species in a local area might underlie this relationship. Frequency-dependent herbivory–whereby mixed-species forests experience less herbivory compared to monocultures (as an extreme example)– is common, especially for oligophagous insect species (Jactel and Brockerhoff 2007). Furthermore, it has been demonstrated that nonhost volatiles reduce attraction of several species of bark beetles to their aggregation pheromones (Seybold et al. 2018), including WPB (Fettig et al. 2005). To that end, combinations of nonhost volatiles and an antiaggregation pheromone have been used successfully to reduce levels of tree mortality attributed to WPB (e.g., Fettig et al. 2012). In general, Hayes et al. (2009) and Fettig et al. (2019) found that measures of host availability explained less variation in mortality than measures of overall tree density, but those conclusions were based on a response variable of "total number of dead host trees," rather than the number of dead host trees conditional on the total number of host trees as in our study (i.e., a binomial response).

The negative relationship between overall tree density, a potential correlate of the local competitive environment, and the probability of ponderosa pine mortality is counter-intuitive but corroborates findings of coincident ground plots (Fettig et al. 2019, in their analysis using proportion of trees killed as a response) and other work during the same hot drought (Restaino et al. 2019). In the absence of management, the forest structure is itself a product of climate and, with increasing importance at finer spatial scales, topographic conditions (Fricker et al. 2019). Thus, the denser forest patches in our study may indicate greater local water availability, more favorable conditions for tree growth and survivorship, and increased resistance to

beetle-induced mortality (Restaino et al. 2019). The negative two-way interaction between site CWD and overall density that amplifies the negative overall density effect in hotter, drier sites (effect size: -0.16; 95% CI: [-0.24, -0.07]) supports this explanation if greater local tree density implies especially favorable growing conditions (and locally resistant trees) when denser patches are found in hot, dry sites.

We found a positive two-way interaction between overall tree density (host and non-host) within each cell and proportion of host trees, which is equivalent to a positive effect of host density (effect size: 0.08; 95% CI: [0.03, 0.12]). The relationship between host density and susceptibility to colonization by bark beetles has been so well-documented at the experimental plot level (e.g., Raffa and Berryman 1987, Oliver 1995) that lowering stand densities through selective harvest of hosts is commonly recommended for reducing future levels of tree mortality attributed to bark beetles (Fettig and Hilszczański 2015), including WPB (Fettig 2016). Greater host density shortens the flight distance required for WPB to disperse to new hosts, which likely facilitates bark beetle spread, however we calibrated our aerial tree detection to ~400 m^2 areas rather than to individual tree locations, so our data are insufficient to address these relationships. Increased density of ponderosa pine, specifically, may disproportionately increase the competitive environment for host trees (and thus increase their susceptibility to WPB colonization) if intraspecific competition amongst ponderosa pine trees is stronger than interspecific competition as would be predicted with coexistence theory (Chesson 2000). Finally, greater host densities increase the frequency that searching WPB land on hosts, rather than nonhosts, thus reducing the amount of energy expended during host finding and selection as well as the time that searching WPB spend exposed to predators.

Negative main effect of host tree mean size, but strong positive interaction with site CWD

Counter to our expectations, we found an overall negative effect of host tree mean size on the probability of host mortality (effect size: -0.40; 95% CI: [-0.46, -0.34]). WPB exhibit a preference for trees 50.8 to 76.2 cm in diameter at breast height (Person 1928, 1931), and a positive relationship between host tree size and levels of tree mortality attributed to WPB was reported by Fettig et al. (2019) in the coincident field plots as well as in other recent studies (Restaino et al. 2019, Stephenson et al. 2019, Pile et al. 2019). Indeed, Fettig et al. (2019) reported no mortality in ponderosa pine trees <10.0 cm DBH attributable to WPB and found no tree size/mortality relationship for incense cedar or white fir in the coincident field plots. These species represent 22.3% of the total tree mortality observed in their study, yet in our study all dead trees were classified as ponderosa pine (see Methods) which could dampen positive effect of tree size on mortality. Larger trees are more nutritious and are therefore ideal targets if local bark beetle density is high enough to successfully initiate mass attack as can occur when many trees are under severe water stress (Bentz et

al. 2010, Kolb et al. 2016). In the recent hot drought, we expected that most trees would be under severe water stress, setting the stage for increasing beetle density, successful mass attacks, and targeting of larger trees. A possible explanation for our finding counter to this expectation is that our observations represent the cumulative mortality of trees during a multi-year drought event and its aftermath. Lower host tree mean size led to a greater probability of host mortality earlier in this drought (Pile et al. 2019, Stovall et al. 2019) and that signal might have persisted even as mortality continued to accumulate driven by other factors. Finally, tree growth rates may be a better predictor of susceptibility to WPB colonization than tree size per se, with slower-growing trees being most vulnerable (Miller and Keen 1960). While slow-growing trees are often also the largest trees, this may not be the case for our study sites especially given the legacy of fire exclusion in the Sierra Nevada and its effect of perturbing forest structure far outside its natural range of variation (Safford and Stevens 2017).

We did observe a strong host tree size effect in its interaction with site CWD (effect size: 0.44; 95% CI: [0.34, 0.54]). In hot, dry sites, larger average host size increased the probability of host mortality while smaller host sizes increased the probability of host mortality in cooler, wetter sites. Notably, a similar pattern was shown by Stovall et al. (2019) with a strong positive tree height/mortality relationship in areas with the greatest vapor pressure deficit and no tree height/mortality relationship in areas with the lowest vapor pressure deficit. Stovall et al. (2019) did not observe that this environmental dependence extended to a negative tree height/mortality relationship (as we did) even at the lowest extremes of their vapor pressure deficit gradient, perhaps because their entire study took place in the southern Sierra Nevada which represents a hotter, drier portion of the more spatially extensive results we present here. Our work suggests that the WPB was cueing into different aspects of forest structure across an environmental gradient in a spatial context in a parallel manner to the temporal context noted by Stovall et al. (2019) and Pile et al. (2019), who observed that mortality was increasingly driven by larger trees as the hot drought proceeded and became more severe.

All of our sites were considered in an "epidemic" population phase for WPB (>5 trees killed per hectare; see Supplemental Information; Miller and Keen 1960, Hayes et al. 2009), but our results challenge the notion that outbreak behavior by the WPB and subsequent tree mortality is always driven by greater tree size. Despite a strong tree size/mortality relationship in coincident ground plots across our study area (Fettig et al. 2019), our results from surveying the broader context surrounding those ground plots reveals different effects of host tree size depending on CWD. Thus, it is possible that the massive tree mortality in hotter/drier Sierra Nevada forests (lower latitudes and elevations; Asner et al. 2016, Young et al. 2017) during the 2012 to 2015 hot drought arose as a synergistic alignment of environmental conditions and local forest structure that allowed WPB to successfully colonize large trees, rapidly increase in population size, and expand. Conversely,

our results may suggest that the unexpectedly low mortality in cooler/wetter Sierra Nevada forests compared to model predictions based on coarser-scale forest structure data (Young et al. 2017) could be explained by a different WPB response to local forest structure due to a lack of an alignment with favorable climate conditions.

Limitations and future directions

We have demonstrated that drones can be effective means of collecting forest data at multiple, vastly different spatial scales to investigate a single, multi-scale phenomenon– from meters in between trees, to hundreds of meters of elevation, to hundreds of thousands of meters of latitude. Some limitations remain but can be overcome with further refinements in the use of this tool for forest ecology. Most of these limitations arise from tree detection and classification uncertainty, and thus it was imperative to work with field data for calibration and uncertainty reporting.

The greatest limitation in our study arising from classification uncertainty is in the assumption that all dead trees were ponderosa pine, which we estimate from coincident field plots is true approximately 73.4% of the time. Because the forest structure factors influencing the likelihood of individual tree mortality during the hot drought depended on tree species (Stephenson et al. 2019), we cannot rule out that some of the ponderosa pine mortality relationships to forest structure that we observed may be partially explained by those relationships in other species that were misclassified as ponderosa pine using our methods. However, the overall community composition across our study area was similar (Fettig et al. 2019) and we are able to reproduce similar forest structure/mortality patterns in drone-derived data when restricting the scope of analysis to only trees detected in the footprints of the coincident field plots with dramatically different patterns observed when including data from the forest surrounding the coincident field plots (see Supplemental information). Thus, we remain confident that the patterns we observed were driven primarily by the dynamic between WPB and ponderosa pine. While spectral information of foliage could help classify living trees to species, the species of standing dead trees were not spectrally distinct. This challenge of classifying standing dead trees to species implies that a conifer forest system with less bark beetle and tree host diversity, such as mountain pine beetle outbreaks in monocultures of lodgepole pine in the Intermountain West, should be particularly amenable to the methods presented here even with minimal further refinement because dead trees will almost certainly belong to a single species and have succumbed to colonization by a single bark beetle species.

Some uncertainty surrounded our ability to detect trees using the geometry of the dense point clouds derived with SfM. The horizontal accuracy of the tree detection was better than the vertical accuracy, which may

result from a more significant error contribution by the field-based calculations of tree height compared to tree position relative to plot center (Table 2). Both the horizontal and vertical accuracy would likely improve with better SfM point clouds, which can be enhanced with greater overlap between images (Frey et al. 2018) or with oblique (i.e., off-nadir) imagery (James and Robson 2014). Frey et al. (2018) found that 95% overlap was preferable for generating dense point clouds in forested areas, and James and Robson (2014) reduced dense point cloud errors using imagery taken at 30 degrees off-nadir. We only achieved 91.6% overlap with the X3 RGB camera and 83.9% overlap with the multispectral camera, and all imagery was nadir-facing. While our live/dead classification was fairly accurate (97.3% on a withheld dataset), our species classifier would likely benefit from better crown segmentation because the pixel-level reflectance values within each crown are averaged to characterize the "spectral signature" of each tree. With better delineation of each tree crown, the mean value of pixels within each tree crown will likely be more representative of that tree's spectral signature. Better crown segmentation might most readily be achieved through greater overlap in imagery. Finally, we anticipate that computer vision and deep learning will prove helpful in overcoming some of these detection and classification challenges (Gray et al. 2019).

Conclusions

Climate change adaptation strategies emphasize management action that considers whole-ecosystem responses to inevitable change (Millar et al. 2007), which requires a macroecological understanding of how phenomena at multiple scales can interact. We've shown that drones can be a valuable tool for investigating multi-scalar phenomena, such as how local forest structure combines with environmental conditions to shape forest insect disturbance. Understanding the conditions that drive dry western U.S. forest responses to disturbances such as bark beetle outbreaks will be vital for predicting outcomes from increasing disturbance frequency and intensity exacerbated by climate change. Our study suggests that outcomes will depend on interactions between local forest structure and broad-scale environmental gradients, with the potential for cross-scale interactions to challenge our current understanding of forest insect dynamics.

References

Anderegg, W. R. L., J. A. Hicke, R. A. Fisher, C. D. Allen, J. Aukema, B. Bentz, S. Hood, J. W. Lichstein, A. K. Macalady, N. McDowell, Y. Pan, K. Raffa, A. Sala, J. D. Shaw, N. L. Stephenson, C. Tague, and M. Zeppel. 2015. Tree mortality from drought, insects, and their interactions in a changing climate. New Phytologist 208:674–683.

Asner, G. P., P. G. Brodrick, C. B. Anderson, N. Vaughn, D. E. Knapp, and R. E. Martin. 2016. Progressive

546 forest canopy water loss during the 2012-2015 California drought. Proceedings of the National Academy of
547 Sciences 113:E249–E255.

548 Baldwin, B. G., A. H. Thornhill, W. A. Freyman, D. D. Ackerly, M. M. Kling, N. Morueta-Holme, and B. D.
549 Mishler. 2017. Species richness and endemism in the native flora of California. American Journal of Botany
550 104:487–501.

551 Bedard, W. D., P. E. Tilden, D. L. Wood, R. M. Silverstein, R. G. Brownlee, and J. O. Rodin. 1969.
552 Western pine beetle: Field response to its sex pheromone and a synergistic host terpene, myrcene. Science
553 164:1284–1285.

554 Bentz, B. J., J. Régnière, C. J. Fettig, E. M. Hansen, J. L. Hayes, J. A. Hicke, R. G. Kelsey, J. F. Negrón,
555 and S. J. Seybold. 2010. Climate change and bark beetles of the western United States and Canada: Direct
556 and indirect effects. BioScience 60:602–613.

557 Berryman, A. A. 1982. Population dynamics of bark beetles. Pages 264–314 *in* Bark Beetles in North
558 American Conifers: A System for the Study of Evolutionary Biology.

559 Brooks, S. P., and A. Gelman. 1998. General methods for monitoring convergence of iterative simulations.
560 Journal of Computational and Graphical Statistics 7:434.

561 Bürkner, P.-C. 2017. **brms**: An *R* package for bayesian multilevel models using *Stan*. Journal of Statistical
562 Software 80:1–28.

563 Byers, J. A., and D. L. Wood. 1980. Interspecific inhibition of the response of the bark beetles, *Dendroctonus*
564 *brevicomis* and *Ips paraconfusus*, to their pheromones in the field. Journal of Chemical Ecology 6:149–164.

565 Chesson, P. 2000. Mechanisms of maintenance of species diversity. Annual Review of Ecology and Systematics
566 31:343–366.

567 Chubaty, A. M., B. D. Roitberg, and C. Li. 2009. A dynamic host selection model for mountain pine beetle,
568 *Dendroctonus ponderosae* Hopkins. Ecological Modelling 220:1241–1250.

569 Clevers, J., and A. Gitelson. 2013. Remote estimation of crop and grass chlorophyll and nitrogen content using
570 red-edge bands on Sentinel-2 and -3. International Journal of Applied Earth Observation and Geoinformation
571 23:344–351.

572 Coops, N. C., M. Johnson, M. A. Wulder, and J. C. White. 2006. Assessment of QuickBird high spatial
573 resolution imagery to detect red attack damage due to mountain pine beetle infestation. Remote Sensing of
574 Environment 103:67–80.

DJI. 2015a. Zenmuse X3 - Creativity Unleashed. https://www.dji.com/zenmuse-x3/info.

DJI. 2015b. DJI - The World Leader in Camera Drones/Quadcopters for Aerial Photography. https://www.dji.com/matrice100/info.

DronesMadeEasy. 2018. Map Pilot for DJI on iOS. https://itunes.apple.com/us/app/map-pilot-for-dji/id1014765000?mt=8.

Evenden, M. L., C. M. Whitehouse, and J. Sykes. 2014. Factors influencing flight capacity of the mountain pine beetle (Coleoptera: Curculionidae: Scolytinae). Environmental Entomology 43:187–196.

Eysn, L., M. Hollaus, E. Lindberg, F. Berger, J.-M. Monnet, M. Dalponte, M. Kobal, M. Pellegrini, E. Lingua, D. Mongus, and N. Pfeifer. 2015. A benchmark of LiDAR-based single tree detection methods using heterogeneous forest data from the alpine space. Forests 6:1721–1747.

Farr, T. G., P. A. Rosen, E. Caro, R. Crippen, R. Duren, S. Hensley, M. Kobrick, M. Paller, E. Rodriguez, L. Roth, D. Seal, S. Shaffer, J. Shimada, J. Umland, M. Werner, M. Oskin, D. Burbank, and D. Alsdorf. 2007. The shuttle radar topography mission. Reviews of Geophysics 45.

Fettig, C. J. 2012. Chapter 2: Forest health and bark beetles. *in* Managing Sierra Nevada Forests. PSW-GTR-237. USDA Forest Service.

Fettig, C. J. 2016. Native bark beetles and wood borers in Mediterranean forests of California. Pages 499–528 *in* Insects and diseases of Mediterranean Forest systems. Springer International Publishing, Switzerland.

Fettig, C. J., and J. Hilszczański. 2015. Management strategies for bark beetles in conifer forests. Pages 555–584 *in* Bark Beetles. Elsevier.

Fettig, C. J., K. D. Klepzig, R. F. Billings, A. S. Munson, T. E. Nebeker, J. F. Negrón, and J. T. Nowak. 2007. The effectiveness of vegetation management practices for prevention and control of bark beetle infestations in coniferous forests of the western and southern United States. Forest Ecology and Management 238:24–53.

Fettig, C. J., S. R. McKelvey, C. P. Dabney, D. P. W. Huber, C. G. Lait, D. L. Fowler, and J. H. Borden. 2012. Efficacy of "Verbenone Plus" for protecting ponderosa pine trees and stands from *Dendroctonus brevicomis* (Coleoptera: Curculionidae) attack in British Columbia and California. Journal of Economic Entomology 105:1668–1680.

Fettig, C. J., S. R. McKelvey, and D. P. W. Huber. 2005. Nonhost angiosperm volatiles and Verbenone disrupt response of western pine beetle, *Dendroctonus brevicomis* (Coleoptera: Scolytidae), to attractant-baited traps. Journal of Economic Entomology 98:2041–2048.

Fettig, C. J., L. A. Mortenson, B. M. Bulaon, and P. B. Foulk. 2019. Tree mortality following drought in the central and southern Sierra Nevada, California, U.S. Forest Ecology and Management 432:164–178.

Flint, L. E., A. L. Flint, J. H. Thorne, and R. Boynton. 2013. Fine-scale hydrologic modeling for regional landscape applications: The California Basin Characterization Model development and performance. Ecological Processes 2:25.

Floyd, M. L., M. Clifford, N. S. Cobb, D. Hanna, R. Delph, P. Ford, and D. Turner. 2009. Relationship of stand characteristics to drought-induced mortality in three Southwestern piñonJuniper woodlands. Ecological Applications 19:1223–1230.

Franceschi, V. R., P. Krokene, E. Christiansen, and T. Krekling. 2005. Anatomical and chemical defenses of conifer bark against bark beetles and other pests. New Phytologist 167:353–376.

Frey, J., K. Kovach, S. Stemmler, and B. Koch. 2018. UAV photogrammetry of forests as a vulnerable process. A sensitivity analysis for a structure from motion RGB-image pipeline. Remote Sensing 10:912.

Fricker, G. A., N. W. Synes, J. M. Serra-Diaz, M. P. North, F. W. Davis, and J. Franklin. 2019. More than climate? Predictors of tree canopy height vary with scale in complex terrain, Sierra Nevada, CA (USA). Forest Ecology and Management 434:142–153.

Gabry, J., D. Simpson, A. Vehtari, M. Betancourt, and A. Gelman. 2019. Visualization in Bayesian workflow. Journal of the Royal Statistical Society: Series A (Statistics in Society) 182:389–402.

Gitelson, A., and M. N. Merzlyak. 1994. Spectral reflectance changes associated with autumn senescence of *Aesculus hippocastanum* L. And *Acer platanoides* L. Leaves. Spectral features and relation to chlorophyll estimation. Journal of Plant Physiology 143:286–292.

Graf, M., M. Reid, B. Aukema, and B. Lindgren. 2012. Association of tree diameter with body size and lipid content of mountain pine beetles. The Canadian Entomologist 144:467–477.

Gray, P. C., A. B. Fleishman, D. J. Klein, M. W. McKown, V. S. Bézy, K. J. Lohmann, and D. W. Johnston. 2019. A convolutional neural network for detecting sea turtles in drone imagery. Methods in Ecology and Evolution 10:345–355.

Griffin, D., and K. J. Anchukaitis. 2014. How unusual is the 2012-2014 California drought? Geophysical Research Letters 41:9017–9023.

Hayes, C. J., C. J. Fettig, and L. D. Merrill. 2009. Evaluation of multiple funnel traps and stand characteristics for estimating western pine beetle-caused tree mortality. Journal of Economic Entomology 102:2170–2182.

633 Hijmans, R. J., J. van Etten, M. Sumner, J. Cheng, A. Bevan, R. Bivand, L. Busetto, M. Canty, D. Forrest,
634 A. Ghosh, D. Golicher, J. Gray, J. A. Greenberg, P. Hiemstra, I. for M. A. Geosciences, C. Karney, M.
635 Mattiuzzi, S. Mosher, J. Nowosad, E. Pebesma, O. P. Lamigueiro, E. B. Racine, B. Rowlingson, A. Shortridge,
636 B. Venables, and R. Wueest. 2019. Raster: Geographic data analysis and modeling.

637 Hunziker, P. 2017. Velox: Fast raster manipulation and extraction.

638 Jactel, H., and E. G. Brockerhoff. 2007. Tree diversity reduces herbivory by forest insects. Ecology Letters
639 10:835–848.

640 Jakubowski, M. K., W. Li, Q. Guo, and M. Kelly. 2013. Delineating individual trees from LiDAR data: A
641 comparison of vector- and raster-based segmentation approaches. Remote Sensing 5:4163–4186.

642 James, M. R., and S. Robson. 2014. Mitigating systematic error in topographic models derived from UAV
643 and ground-based image networks. Earth Surface Processes and Landforms 39:1413–1420.

644 Kane, V. R., M. P. North, J. A. Lutz, D. J. Churchill, S. L. Roberts, D. F. Smith, R. J. McGaughey, J. T.
645 Kane, and M. L. Brooks. 2014. Assessing fire effects on forest spatial structure using a fusion of Landsat and
646 airborne LiDAR data in Yosemite National Park. Remote Sensing of Environment 151:89–101.

647 Kolb, T. E., C. J. Fettig, M. P. Ayres, B. J. Bentz, J. A. Hicke, R. Mathiasen, J. E. Stewart, and A. S. Weed.
648 2016. Observed and anticipated impacts of drought on forest insects and diseases in the United States. Forest
649 Ecology and Management 380:321–334.

650 Kuhn, M. 2008. Building predictive models in R using the caret package. Journal of Statistical Software
651 28:1–26.

652 Larson, A. J., and D. Churchill. 2012. Tree spatial patterns in fire-frequent forests of western North America,
653 including mechanisms of pattern formation and implications for designing fuel reduction and restoration
654 treatments. Forest Ecology and Management 267:74–92.

655 Li, W., Q. Guo, M. K. Jakubowski, and M. Kelly. 2012. A new method for segmenting individual trees from
656 the LiDAR point cloud. Photogrammetric Engineering & Remote Sensing 78:75–84.

657 Logan, J. A., P. White, B. J. Bentz, and J. A. Powell. 1998. Model analysis of spatial patterns in mountain
658 pine beetle outbreaks. Theoretical Population Biology 53:236–255.

659 Meyer, F., and S. Beucher. 1990. Morphological segmentation. Journal of Visual Communication and Image
660 Representation 1:21–46.

661 Micasense. 2015. MicaSense. https://support.micasense.com/hc/en-us/articles/215261448-RedEdge-User-Manual-PDF-Downl

Millar, C. I., N. L. Stephenson, and S. L. Stephens. 2007. Climate change and forests of the future: Managing in the face of uncertainty. Ecological Applications 17:2145–2151.

Millar, C. I., R. D. Westfall, D. L. Delany, M. J. Bokach, A. L. Flint, and L. E. Flint. 2012. Forest mortality in high-elevation whitebark pine (*Pinus albicaulis*) forests of eastern California, USA: Influence of environmental context, bark beetles, climatic water deficit, and warming. Canadian Journal of Forest Research 42:749–765.

Miller, J. M., and F. P. Keen. 1960. Biology and control of the western pine beetle: A summary of the first fifty years of research. US Department of Agriculture.

Moeck, H. A., D. L. Wood, and K. Q. Lindahl. 1981. Host selection behavior of bark beetles (Coleoptera: Scolytidae) attacking *Pinus ponderosa*, with special emphasis on the western pine beetle, *Dendroctonus brevicomis*. Journal of Chemical Ecology 7:49–83.

Morris, J. L., S. Cottrell, C. J. Fettig, W. D. Hansen, R. L. Sherriff, V. A. Carter, J. L. Clear, J. Clement, R. J. DeRose, J. A. Hicke, P. E. Higuera, K. M. Mattor, A. W. R. Seddon, H. T. Seppä, J. D. Stednick, and S. J. Seybold. 2017. Managing bark beetle impacts on ecosystems and society: Priority questions to motivate future research. Journal of Applied Ecology 54:750–760.

Oliver, W. W. 1995. Is self-thinning in ponderosa pine ruled by *Dendroctonus* bark beetles? Page 6 *in* Forest health through silviculture: Proceedings of the 1995 National Silviculture Workshop.

Pau, G., F. Fuchs, O. Sklyar, M. Boutros, and W. Huber. 2010. EBImage: An R package for image processing with applications to cellular phenotypes. Bioinformatics 26:979–981.

Person, H. L. 1928. Tree selection by the western pine beetle. Journal of Forestry 26:564–578.

Person, H. L. 1931. Theory in explanation of the selection of certain trees by the western pine beetle. Journal of Forestry 29:696–699.

Pile, L. S., M. D. Meyer, R. Rojas, O. Roe, and M. T. Smith. 2019. Drought impacts and compounding mortality on forest trees in the southern Sierra Nevada. Forests 10:237.

Plowright, A. 2018. ForestTools: Analyzing remotely sensed forest data.

Raffa, K. F., B. H. Aukema, B. J. Bentz, A. L. Carroll, J. A. Hicke, M. G. Turner, and W. H. Romme. 2008. Cross-scale drivers of natural disturbances prone to anthropogenic amplification: The dynamics of bark beetle eruptions. BioScience 58:501–517.

Raffa, K. F., and A. A. Berryman. 1983. The role of host plant resistance in the colonization behavior and ecology of bark beetles (Coleoptera: Scolytidae). Ecological Monographs 53:27–49.

Raffa, K. F., and A. A. Berryman. 1987. Interacting selective pressures in conifer-bark beetle systems: A basis for reciprocal adaptations? The American Naturalist 129:234–262.

Raffa, K. F., J.-C. Grégoire, and B. Staffan Lindgren. 2015. Natural history and ecology of bark beetles. Pages 1–40 *in* Bark Beetles. Elsevier.

R Core Team. 2018. R: A language and environment for statistical computing. R Foundation for Statistical Computing, Vienna, Austria.

Restaino, C., D. Young, B. Estes, S. Gross, A. Wuenschel, M. Meyer, and H. Safford. 2019. Forest structure and climate mediate drought-induced tree mortality in forests of the Sierra Nevada, USA. Ecological Applications 0:e01902.

Rouse, W., R. H. Haas, W. Deering, and J. A. Schell. 1973. Monitoring the vernal advancement and retrogradation (green wave effect) of natural vegetation. Type II Report, Goddard Space Flight Center, Greenbelt, MD, USA.

Roussel, J.-R. 2019. lidRplugins: Extra functions and algorithms for lidR package.

Roussel, J.-R., D. Auty, F. De Boissieu, and A. S. Meador. 2019. lidR: Airborne LiDAR data manipulation and visualization for forestry applications.

Safford, H. D., and J. T. Stevens. 2017. Natural range of variation for yellow pine and mixed-conifer forests in the Sierra Nevada, Southern Cascades, and Modoc and Inyo National Forests, California, USA. Page 241.

dos Santos, A. A., J. Marcato Junior, M. S. Araújo, D. R. Di Martini, E. C. Tetila, H. L. Siqueira, C. Aoki, A. Eltner, E. T. Matsubara, H. Pistori, R. Q. Feitosa, V. Liesenberg, and W. N. Gonçalves. 2019. Assessment of CNN-Based Methods for Individual Tree Detection on Images Captured by RGB Cameras Attached to UAVs. Sensors (Basel, Switzerland) 19.

Seidl, R., J. Müller, T. Hothorn, C. Bässler, M. Heurich, and M. Kautz. 2016. Small beetle, large-scale drivers: How regional and landscape factors affect outbreaks of the European spruce bark beetle. The Journal of applied ecology 53:530–540.

Seybold, S. J., B. J. Bentz, C. J. Fettig, J. E. Lundquist, R. A. Progar, and N. E. Gillette. 2018. Management of western North American bark beetles with semiochemicals. Annual Review of Entomology 63:407–432.

Shepherd, W. P., D. P. W. Huber, S. J. Seybold, and C. J. Fettig. 2007. Antennal responses of the western pine beetle, Dendroctonus brevicomis (Coleoptera: Curculionidae), to stem volatiles of its primary host, Pinus ponderosa, and nine sympatric nonhost angiosperms and conifers. Chemoecology 17:209–221.

Shiklomanov, A. N., B. A. Bradley, K. M. Dahlin, A. M. Fox, C. M. Gough, F. M. Hoffman, E. M. Middleton, S. P. Serbin, L. Smallman, and W. K. Smith. 2019. Enhancing global change experiments through integration of remote-sensing techniques. Frontiers in Ecology and the Environment 0.

Shin, P., T. Sankey, M. Moore, and A. Thode. 2018. Evaluating unmanned aerial vehicle images for estimating forest canopy fuels in a ponderosa pine stand. Remote Sensing 10:1266.

Stephenson, N. 1998. Actual evapotranspiration and deficit: Biologically meaningful correlates of vegetation distribution across spatial scales. Journal of Biogeography 25:855–870.

Stephenson, N. L., A. J. Das, N. J. Ampersee, and B. M. Bulaon. 2019. Which trees die during drought? The key role of insect host-tree selection. Journal of Ecology:75.

Stovall, A. E. L., H. Shugart, and X. Yang. 2019. Tree height explains mortality risk during an intense drought. Nature Communications 10:1–6.

Thistle, H. W., H. Peterson, G. Allwine, B. Lamb, T. Strand, E. H. Holsten, and P. J. Shea. 2004. Surrogate pheromone plumes in three forest trunk spaces: Composite statistics and case studies. Forest Science 50.

USDAFS. 2019, February 11. Press Release: Survey finds 18 million trees died in California in 2018. https://www.fs.usda.gov/Internet/FSE_DOCUMENTS/FSEPRD609321.pdf.

Vega, C., A. Hamrouni, S. El Mokhtari, J. Morel, J. Bock, J. P. Renaud, M. Bouvier, and S. Durrieu. 2014. PTrees: A point-based approach to forest tree extraction from LiDAR data. International Journal of Applied Earth Observation and Geoinformation 33:98–108.

Weinstein, B. G., S. Marconi, S. Bohlman, A. Zare, and E. White. 2019. Individual Tree-Crown Detection in RGB Imagery Using Semi-Supervised Deep Learning Neural Networks. Remote Sensing 11:1309.

Wyngaard, J., L. Barbieri, A. Thomer, J. Adams, D. Sullivan, C. Crosby, C. Parr, J. Klump, S. Raj Shrestha, and T. Bell. 2019. Emergent challenges for science sUAS data management: Fairness through community engagement and best practices development. Remote Sensing 11:1797.

Young, D. J. N., J. T. Stevens, J. M. Earles, J. Moore, A. Ellis, A. L. Jirka, and A. M. Latimer. 2017. Long-term climate and competition explain forest mortality patterns under extreme drought. Ecology Letters 20:78–86.

Zhang, W., J. Qi, P. Wan, H. Wang, D. Xie, X. Wang, and G. Yan. 2016. An easy-to-use airborne LiDAR data filtering method based on cloth simulation. Remote Sensing 8:501.